Resolving minute temporal seismic velocity changes induced by earthquake damage: The more stations, the merrier ?
Pre-print submitted to EarthArXiv. It is currently under peer-review :)

Luc Illien[1,2], Christoph Sens-Schönfelder[1], Kuan-Yu Ke[1,3]

[1] *Helmholtz Center, German Center for Geosciences GFZ, Potsdam, Germany*
[2] *Department of Geosciences, Potsdam Universität, Potsdam, Germany*
[3] *Insitut fur geologische Wissenschaften, Freie Universität Berlin, Berlin, Germany*

17 October 2022

SUMMARY

Ground shaking induced by earthquakes often introduces transient changes in seismic velocity monitored with ambient noise. These changes are usually attributed to relaxation behavior following the co-seismic damage in the subsurface and are of relevance for postseismic hazard mitigation. However, the velocity evolution associated with this phenomenon can occur at very small timescales and amplitudes that are not resolved with seismic interferometry and are therefore challenging to link to laboratory experiments. A way to improve the temporal resolution of the velocity time-series is to test whether the estimation of the relative seismic velocity changes dv/v obeys the ergodic hypothesis in which the joint use of co-located stations would lead to better resolved measurements. In this study, we present results from a dense seismic array that was deployed for two weeks at the remarkable Patache site in Chile. Thanks to high temporal averaging capabilities, we are able to resolve seismic velocity changes in the 3-6 Hz frequency band at a 10-minutes resolution around the occurrence of a moderate earthquake (PGV $\sim$ 1 cm/s). We report a velocity drop of $\sim$0.4% in the first 10 minutes after ground shaking. Half of this initial drop was recovered within the two following days. The shape of the recovery follows a log-linear shape over the whole observed recovery phase, analogous to slow dynamics experiments. When normalised by the total amount of processed data, we show that the ergodic hypothesis almost perfectly holds in our network: the dv/v signal to noise ratio (SNR) obtained when averaging a few observation with large stacking durations for the correlation functions is almost equal to the SNR when using a large number of observations with small stacking durations. To understand if the ergodicity is linked to a particular site property, we use the array capabilities to identify the surf at the shoreline as the source of the noise and to derive a 1D shear velocity profile with the focal spot imaging technique and a transdimensional Bayesian inversion framework. The inversion shows that hard rocks lie close to the surface indicating that this material hosts the observed shallow velocity changes. We discuss our high-resolution measurements and attribute them to a stable noise source excited by the shore, the ergodicity property and an ideal subsurface structure. Finally, we discuss the effect of moderate earthquakes on subsurface damage and the potential relaxation processes in hard rocks.

Key words: seismic interferometry - earthquake damage - relaxation - slow dynamics - ambient noise - ergodicity - seismic velocity - nonlinear elasticity

1 INTRODUCTION

Monitoring of seismic velocity changes obtained from ambient noise cross-correlations is now a widely used technique among seismologists. Because the seismic velocity in rocks is sensitive to many driving processes, this tool has been used to constrain various dynamics in the subsurface such as changes in groundwater (Lecocq et al. 2017; Gassenmeier et al. 2015; Clements & Denolle 2018; Illien et al. 2021), soil moisture (Dietze et al. 2020; Oakley et al. 2021), permafrost thickness (Overduin et al. 2015; Al-baric et al. 2021; Lindner et al. 2021) and volcanic activity (Sens-Schönfelder et al. 2014; Budi-Santoso & Lesage 2016; Donaldson et al. 2019). The use of seismic interferometry has also enabled the study of rock properties changes in response to in-situ strain induced by surface temperature (Richter et al. 2014; Lecocq et al. 2017), Earth tides (Takano et al. 2014; Sens-Schönfelder & Eulenfeld 2019) and more notably to dynamic strain due to ground shaking during earthquakes. Indeed, there is a plethora of seismic interferometry studies that were conducted following major earthquakes

(Brenguier et al. 2008; Nakata & Snieder 2012; Viens et al. 2018; Qin et al. 2020). Most of this literature shows two distinct phases: a short co-seismic phase in which the seismic velocity drops and a post-seismic phase in which the velocity recovers in a non-linear fashion. This latter phase is called relaxation or slow dynamics and can last for several years (Brenguier et al. 2008; Marc et al. 2021). These time-dependent changes of the seismic velocity suggests that earthquakes induce a lingering effect in subsurface rock properties. This mechanical perturbation may be at the origin of other transient surface observations, which exhibit a similar time-evolution such as transient increases of aquifer permeability (Manga et al. 2012; Illien et al. 2021) or landslide rates (Marc et al. 2015).

The time dependency of the elastic behaviour is linked to a non-classical type of elastic non-linearity. This behaviour has been reproduced experimentally in a wide range of materials ranging from rocks (TenCate et al. 2000; Brantut 2015; Shokouhi et al. 2017a) over concrete (Bekele et al. 2017) to unconsolidated granular samples (Knight et al. 1995), which suggests that this phenomena is universal (Snieder et al. 2016). The transient dynamics is generally interpreted as the result of *1)* a phase of "damage" during deformation that arises from a variety of contacts (Ostrovsky et al. 2019; Sens-Schönfelder et al. 2019) which are broken at grain boundaries or at defect locations and *2)* a phase of "healing" associated with thermally activated processes that bring the metastable contacts towards a new equilibrium state – a phase also called slow dynamics or relaxation (Guyer et al. 1999; TenCate et al. 2000). In rocks and near-surface geomaterials, this contact recovery is thought to happen due to micro-cracks and fracture closure (Meyer et al. 2021) or re-arrangement of frictional shear zones (Lieou et al. 2017) and with a large contribution of chemical processes modulated by moisture (Brantut 2015; Bittner & Popovics 2021; Gao et al. 2022). Corresponding physical and phenomenological models can be developed from laboratory observations thanks to a fine control of the strain disturbance (Remillieux et al. 2017), a well-resolved temporal acoustic monitoring system (that can observe relaxation timescales down to fractions of a second (Shokouhi et al. 2017b)), simplified geometries (Yoritomo & Weaver 2020) or the knowledge of the physical properties of the chosen rock samples. However, the application of models to field observations is challenging due to poorly resolved velocity measurements, superimposed influences and depth-dependent properties. Indeed, the stochastic nature of the seismic ambient noise wavefield requires temporal stacking of the noise correlations to recover the stable pseudo Green's function that is required for velocity monitoring (Xu et al. 2021). This reconstruction controls the final time-resolution of the obtained dv/v measurements. Moreover, constraints on the subsurface structure and velocity are rarely available. These limitations prevent us from answering fundamental questions that would bridge the gap between field observations and models, which includes *what is the impact of small/moderate shaking perturbation*, *what is the shortest relaxation timescale in the field* or *in which structures/rocks the relaxation is likely to occur in the subsurface?*

To address these questions, we performed seismic interferometry study using a dense seismic array in Patache, Chile (Fig. 1) located around the permanent station PATCX in the IPOC network. This station has produced remarkable results with observations of stable velocity changes induced by the Earth's tides (Sens-Schönfelder & Eulenfeld 2019), earthquakes (Gassenmeier et al. 2016) or temperature (Richter et al. 2014). The relative success of these studies suggests that the conditions at this site are particularly suited for monitoring studies. In this paper, we attempt to investi-

gate these specific conditions and increase the time-resolution of the velocity changes retrieval at Patache with the ergodic hypothesis (Moore 2015): We assume that the average statistical properties of the diffuse noise wavefield across the dense network (the ensemble average) during a short time interval at time t is similar to the average statistical properties recorded at one station over a larger time span (the time average). If this assumption holds, by spatially averaging the results obtained from co-located stations, one can significantly reduce the time window needed for stacking correlation functions and therefore improve the time-resolution of stable velocity change measurement δv. This hypothesis has been made implicitly in previous studies (Sens-Schönfelder et al. 2014; Illien et al. 2022) but not tested. Here, we address the validity of this assumption explicitly.

Using this technique, we report stable observations of velocity changes at a 10-minute resolution for a period of $\sim$ two weeks. During this interval, we measure a co-seismic velocity drop of 0.4 % amplitude and a well-resolved subsequent recovery in the 3-6 Hz frequency band. Utilising the dense network, we also compute the local Rayleigh wave dispersion curve using the focal spot imaging technique. We invert the obtained results for a 1D shear velocity profile using transdimensional Bayesian inversion and show that the relaxation changes are hosted in a hard rock site. The characterisation of the site also allows to highlight advantageous conditions for stable dv/v measurements.

We describe the data and methods in section 2. In section 3.1 and 3.2, we present the seismic velocity changes results and the inferred 1D shear velocity profile obtained at our field site. Section 4 is dedicated to the discussion, notably on the stability of the velocity estimates and the relaxation processes in hard rocks. Conclusions are in section 5.

2 DATA AND METHODS

2.1 The Peso array

The Peso array consists of 15 geophones (3-components) located around the broadband station PATCX of the Chilean IPOC network (GFZ Potsdam & CNRS-INSU (2006), Fig. 1). Stations were installed on the 21st of October 2018 with nine stations recording for $\sim$ two weeks while the others were relocated after $\sim$ 1.5 days . The array geometry was designed in a circular-triangular pattern to maximise different inter-station distances and optimize the usability for different tasks such as the study of the noise sources, the investigation of the subsurface velocity structure and the monitoring of velocity changes. Placed on top of an escarpment located at 70 km south of Iquique city (Fig. 1, Fig. S1), the stations have an elevation of about 600 m above sea level. After performing a beam-forming anaylsis (method in Text S1), we estimate that the array is strongly dominated by waves propagating in the network from the south-west direction with a slowness of 0.65 s/km (Fig 1c).

2.2 Seismic interferometry for retrieving relative seismic velocity changes

We compute ambient noise cross-correlations to estimate relative seismic velocity changes dv/v (Sens-Schönfelder & Brenguier 2019) using the stations that were installed for two weeks (9 stations) and the permanent station PATCX (Fig. 1). We first preprocess the seismic traces to limit the effect of high-amplitudes arrivals
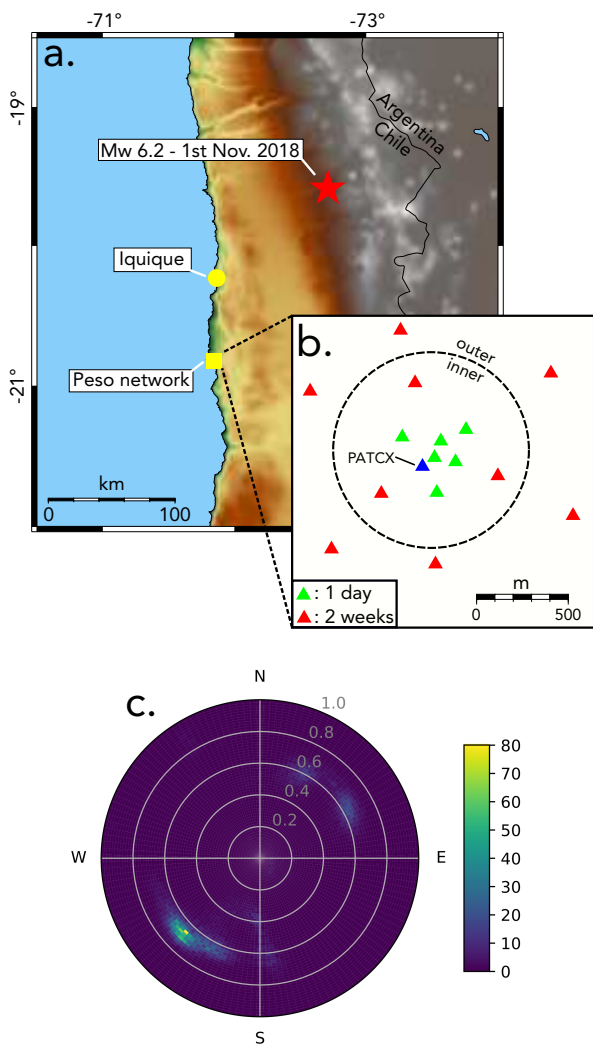
Figure 1. *Map of the study area and beamforming analysis.* **a.** Location of the PESO array relative to Chile. The red star indicates the epicenter of the 1st of November 2018 earthquake. **b.** Geometric setting of the PESO array. The blue triangle stands for the permanent PATCX station. The circle indicates our convention for the inner ring and the outer ring for this study **c.** Results of the beamforming analysis. Colorbar indicates the energy level that is reported on the azimuthal plot.

such as earthquakes on the correlations. These signals are numerous in the seismically active continental margin of northern Chile due to many small earthquakes (Gassenmeier et al. 2016; Sens-Schönfelder & Eulenfeld 2019). To minimise unphysical bias introduced by non-linear normalisation schemes such as the 1-bit normalisation or spectral whitening (Fichtner et al. 2017), we choose a statistical approach to identify the time segments which contain the short-term high amplitudes and remove them from the analysis.

Due to its multiple scattering nature, the recorded seismic wavefield follows a Gaussian probability distribution (Groos & Ritter 2009). The amplitudes of the envelope of such a field are Rayleigh-distributed. The corresponding distribution is defined by a single scale parameter β (McNicol 1949; Oshima & Takenaka 2020):

$$p(a) = \frac{a}{\beta^2} \exp\left(\frac{a^2}{2\beta^2}\right) \tag{1}$$

where $p(a)$ denotes the probability density of the envelope amplitudes a.

The ballistic arrivals and coda waves induced by a seismic event or a local disturbance unavoidably superpose on the background noise and increase the amplitude of the recorded field, changing the scale parameter β. Our approach consists of building amplitude predictions based on an estimate of β dominated by the background noise and compare it to short-term estimates of the mean squared envelope that are dominated by large transient amplitudes.

In a first step, we filter the seismograms and compute the envelopes $a(t)$ using the Hilbert transform. The mean of the logarithm of the envelope is linked to the scale parameter β through the log-Rayleigh distribution (Rivet et al. 2007). Since the mean of the logarithm down-weights large amplitude samples, we obtain an estimate of β that characterises the amplitude of the background field. According to Rivet et al. (2007), β can be retrieved from the following relationship:

$$\beta_1 = \exp\left[\overline{\ln a(t)} - \frac{1}{2}(\ln 2 - \gamma)\right] \tag{2}$$

In this equation, γ is the Euler's constant and $\overline{\ln a(t)} = 1/N \sum_i \ln(a_i)$ is the logarithm of the geometric mean. Corresponding computations were performed in 1-hour segments to down-weight furthermore the short-lived high amplitudes of earthquakes or other local disturbances. The assumption is that these disturbances, despite potentially being orders of magnitudes larger than the background, do not significantly bias this estimate of β due to the logarithm and the long term averaging. β_1 can be used as a prediction of background amplitude even if perturbations superpose the recorded signal.

In a second step, we obtain a short term estimate over 1-minute time windows of β with the intention to identify the high amplitude disturbances. Therefore, we estimate β from the mean squared envelope (McNicol 1949):

$$\beta_2 = \sqrt{2 \, \overline{a^2}} \tag{3}$$

with $\overline{a^2} = 1/N \sum_i a_i^2$ being the arithmetic average of the squared envelope. If the seismic signal is Rayleigh-distributed with a stationary scale parameter, the two estimates β_1 and β_2 will be equal. Short disturbances superposing the background signal are very well discriminated by the ratio β_2/β_1 even for fairly small additional signals.

We illustrate this process in Fig. 2 by comparing the amplitude of the signal, the predicted background signal amplitude derived from β_1 and the short term high amplitude estimate derived from β_2. To identify segments containing disturbances, we calculate the ratio of β_2/β_1 and compare it to a threshold value I that we set equal to 1.6 based on visual inspection of the performance. We construct a mask that we set to zero for all 1-minute segments with $\beta_2/\beta_1 > I$ and to 1 otherwise (Fig. 2b). In a last step, we taper the edges of the mask and save it to a file. We build masks for every station of the network using the vertical component filtered in a narrow band centered at 4Hz. On average, we found that 10 to 40% of the seismic traces were muted depending on the day and the station considered (Fig. S2).

Following the previous calculations, we trim the traces to 1-minute segments and resample the data at 50 Hz. We taper and filter the data in the 3-6 Hz frequency band. This band was chosen because of the stable results it has provided in previous studies at this site (Richter et al. 2014; Gassenmeier et al. 2016; Sens-Schönfelder & Eulenfeld 2019). Finally, we mute the raw traces with the com-
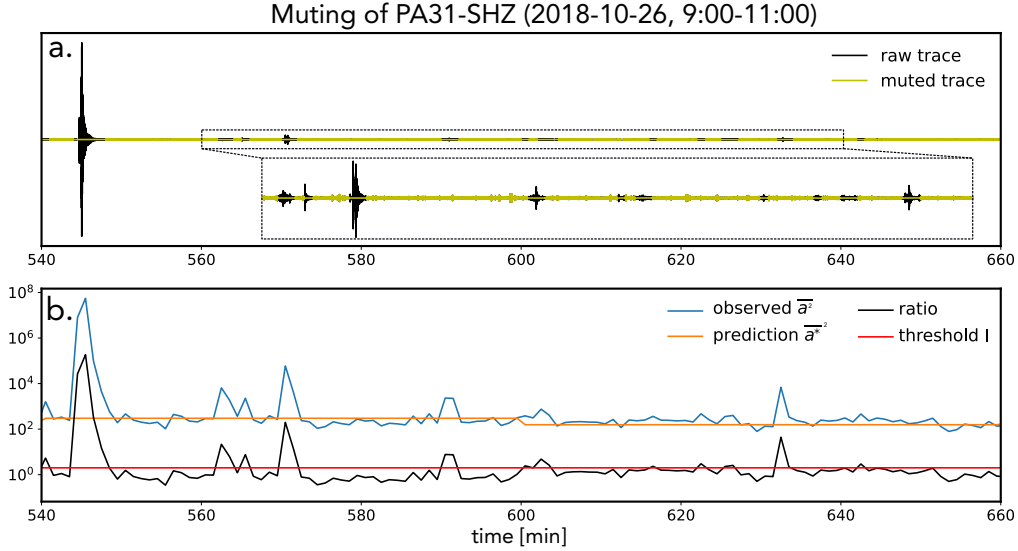
Figure 2. *Muting of the seismic trace, an example.* **a.** The black trace shows two hours of vertical data at the station PA31. The other trace stands for the muted version with a close-up for clarity. **b.** The blue line indicates the estimates of β_2 based on the average squared envelope of the raw trace shown in **a** at a 1-minute resolution. Orange line shows the prediction of β_1 based on the squared envelope predicted by the log-Rayleigh distribution at each hour. The ratio of the observation and the prediction is shown in black with the red line indicating the threshold used for muting the raw trace.

puted masks (Fig. 2). We calculate all possible cross-correlation combinations which include all autocorrelations AC (ZZ, EE, NN, 30 combinations), single station cross-correlations SC (ZN, ZE, EN, 30 combinations) and interstation cross-correlations CC (9 components cross-correlation tensor after rotation for 405 combinations). We cross-correlate the 1-minute segments and stack the results over intervals of 10 minutes.

To estimate the average relative velocity changes dv/v, we use the *stretching* technique (Sens-Schönfelder & Wegler 2006), assuming the velocity changes are spatially homogeneous. For each combination, we compute the stretched versions of the correlation functions $C(t_i, \tau)$ where t_i is the date and τ is the lapse time of the correlation function. We use the 7 to 16 seconds lapse time window ($[\tau_1, \tau_2]$) and compare them to a unique reference ξ_r that is taken as the average cross-correlation function of the whole time period. This allow us to form the similarity matrix with ε_j being the stretching factor:

$$R_r(t_i, \varepsilon_j) = \int_{\tau_1}^{\tau_2} C(t_i, \tau)\xi_r(\tau * (1 + \varepsilon_j))\mathrm{d}\tau. \tag{4}$$

These similarity matrices $R_r(t_i, \varepsilon_j)$ can be all stacked to obtain the final dv/v representative for the entire field site (Fig. S3). Details for calculations can be found in Illien et al. (2021) in which we used the same computation scheme for the velocity changes estimation.

2.3   Estimation of the Rayleigh wave dispersion curve

To constrain the range of absolute velocities in which the relative changes dv/v occur and resolve the subsurface structure at our field site, we estimate the average 1D Rayleigh wave dispersion curve. We use the data recorded on the 22nd of October by the 16 stations network (Fig. 1) to maximize the number of available interstation distances. We preprocess the traces by correcting for the instrument responses, filtering in the 0.25-16 Hz range and muting high-amplitudes arrivals with the technique described in section 2.2.

We use the focal spot imaging technique to obtain Rayleigh wave phase velocities (Hillers et al. 2016). This technique is based on the spatial width of the zero lag cross-correlation field and aims to reconstruct the high-amplitude focal spot that emerges due to time-reversal properties (Conti et al. 2002; Fink 2008). To normalise amplitudes between the different stations, we compute in the Fourier domain the cross-coherence γ. For two stations A and B, we have

$$\gamma_{AB}(w) = \frac{u_A(w)u_B^*(w)}{|u_A(w)||u_B(w)|} \tag{5}$$

with u_A and u_B being the waveforms recorded at stations A and B and w the angular frequency. We perform the computation on hourly segments and stack the 24 resulting cross-coherence functions of the 22nd of October for each ZZ interstation combination. We assume that the wavefield is dominated by Rayleigh waves. In this case, the cross-coherence amplitudes at the zero lag time τ (for ZZ combinations) can be expressed as (Hillers et al. 2016)

$$A(r, \tau = 0) \sim \sigma J_0(kr)e^{-\alpha r}. \tag{6}$$

In this equation, r is the interstation distance, k is the wavenumber, σ is a scaling constant that accounts for the preprocessing and α is an apparent attenuation coefficient. J_0 is the Bessel function of the first kind. The first zero crossing of equation (6), which determines the size of the focal spot, is located at

$$r^0 = \frac{3}{8}\lambda \tag{7}$$

and therefore completely determines the wavelength λ. From fitting relation (6), one can see that phase velocities for different frequencies can be obtained with a suitable interstation distance coverage r. To obtain w, we apply a 0.5 Hz wide bandpass filter on the cross-coherence functions centered around target frequencies between 0.5 Hz and 2.75 Hz with a frequency increment of 0.25 Hz. We fit the data in a procedure similar to Hillers et al. (2016): we first use all the available amplitudes to obtain a first estimate for the wavelength λ (red lines in Fig. 3). Then, we fit the
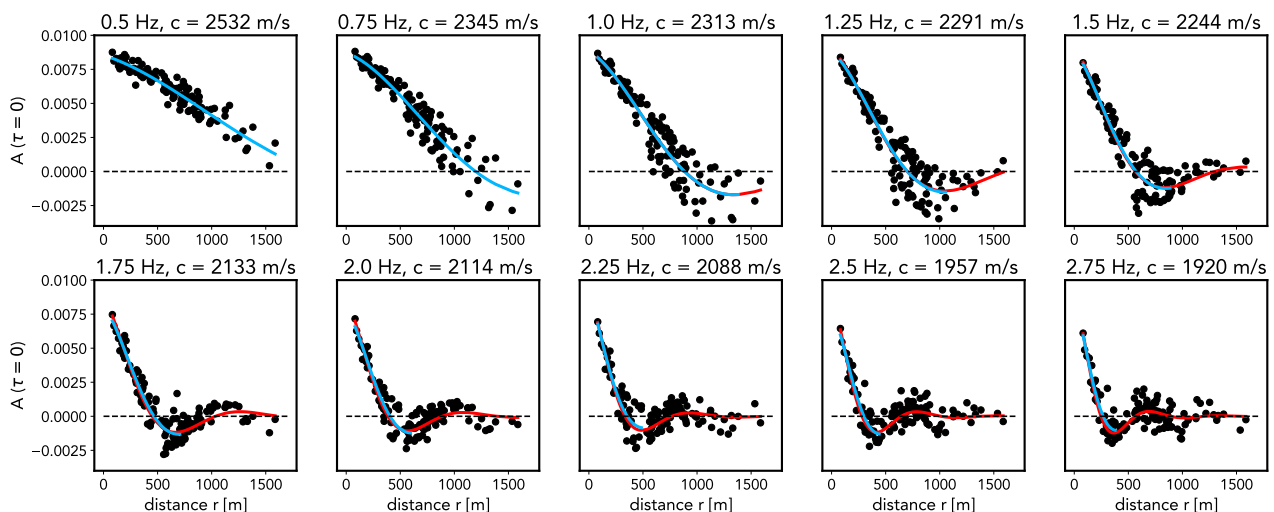
Figure 3. *Focal spot fitting results.* Each plot indicates the result from a different central frequency (indicated in the titles with the corresponding inferred phase velocity). Y-axis represents the amplitude of the cross-coherence ZZ functions at zero lag time while the x-axis shows the interstation distance. Red and blue lines show the fitting from the first iteration and second iteration respectively. Dashed lines indicate the 0 amplitude.

combinations that are within the first 0.7 λ (green lines in Fig. 3) to obtain a second improved estimate: At distances larger than one wavelength, the estimation can be contaminated by scattering and topography effects (Hillers et al. 2016), hence we estimate the velocity closer to the first 0 crossing. We obtain 10 measures for the dispersion curve that we re-interpolate to 20 data points with the Geopsy software.

2.4 Inversion of the 1D shear velocity profile

We invert the dispersion curve with BayHunter (Dreiling & Tilmann 2019; Dreiling et al. 2020), a python package dedicated to Markov chain Monte Carlo transdimensional Bayesian inversion. The main advantage of a Bayesian inversion is the retrieval of an ensemble of models and a better assessment of uncertainties in the retrieved solutions. Another advantage is that the model complexity i.e the number of layers (hence *transdimensional*) and the noise in the data are unknown hyper-parameters that are determined during the inversion process. For more details regarding the algorithm, we refer the reader to the paper of Bodin et al. (2012) and the documentation of BayHunter (Dreiling & Tilmann 2019).

In this paper, we focus on estimating a shear-velocity profile and the V_P/V_S ratio. We give a range of possible solutions for these physical parameters and the hyper-parameters as priors for the inversion (Table 1). 50 Monte-Carlo chains are initialized to explore enough possibilities in the parameter space, using a total of 772608 iterations with a 2:1 ratio between the burn-in phase (initial exploration) and the exploration phase in which we look for the possible models. Some of the chains fail to converge as they return significantly smaller likelihoods than most chains after the burn-in phase: The threshold controlling the convergence is a percentage (here taken as 95%) of the maximum reached median likelihood from the chain ensemble. The chains not reaching this median likelihood are declared outlier chains. The final posterior distribution gathers 100,000 models by subsampling all non-outlier chains. We interpolate the results at a 50 m resolution.

Vs [km/s]	(0.5, 4)
z [km]	(0, 1)
number layers	(1, 12)
Vp/Vs	(1.5, 2.2)
noise [km/s]	(1e-4, 1e-1)

Table 1. Parameters priors used in the inversions.

3 RESULTS

3.1 Relative Seismic Velocity changes

3.1.1 The dv/v time-series

Measurements of relative seismic velocity changes for each individual cross-correlation combination appear to be strongly scattered, although the measurements converge towards a clear dynamics when all plotted together (black dots, Fig. 4a). To illustrate the precision that can be obtained with a single station we show the measurements jointly obtained using the six possible combinations of the permanent station PATCX (autocorrelations and single-station cross-correlations) with the blue curve in Fig. 4a. The highest precision is obtained when using all combinations in the network, reducing the noise to an apparent $\sim$ 0.05% (red line, Fig. 4). For all measurements, we observe periods with larger scatter that we attribute to changes in the noise wavefield. These changes are seen in the traces amplitudes computed when building the pre-processing masks (Fig. 4b). We attribute the larger amplitudes (obtained here at 4 Hz) to strong winds in the afternoon.

We observe little to no velocity changes from the 22nd of October to the 1st of November. A clear drop of $\sim$0.4% is then visible and simultaneous with the Mw 6.2 earthquake that occurred at $\sim$ 150 km from the array (Fig. 1a). Averaging all horizontal component envelopes in our network, we measure a ground shaking intensity of the event to $\sim$1 cm/s PGV (Fig. S4). Half of the initial velocity drop was recovered after two days, with strongest recovery at early times after the co-seismic drop. The duration of our data is not sufficient to see a full recovery, hence reduced velocities appeared sustained for the observation time.
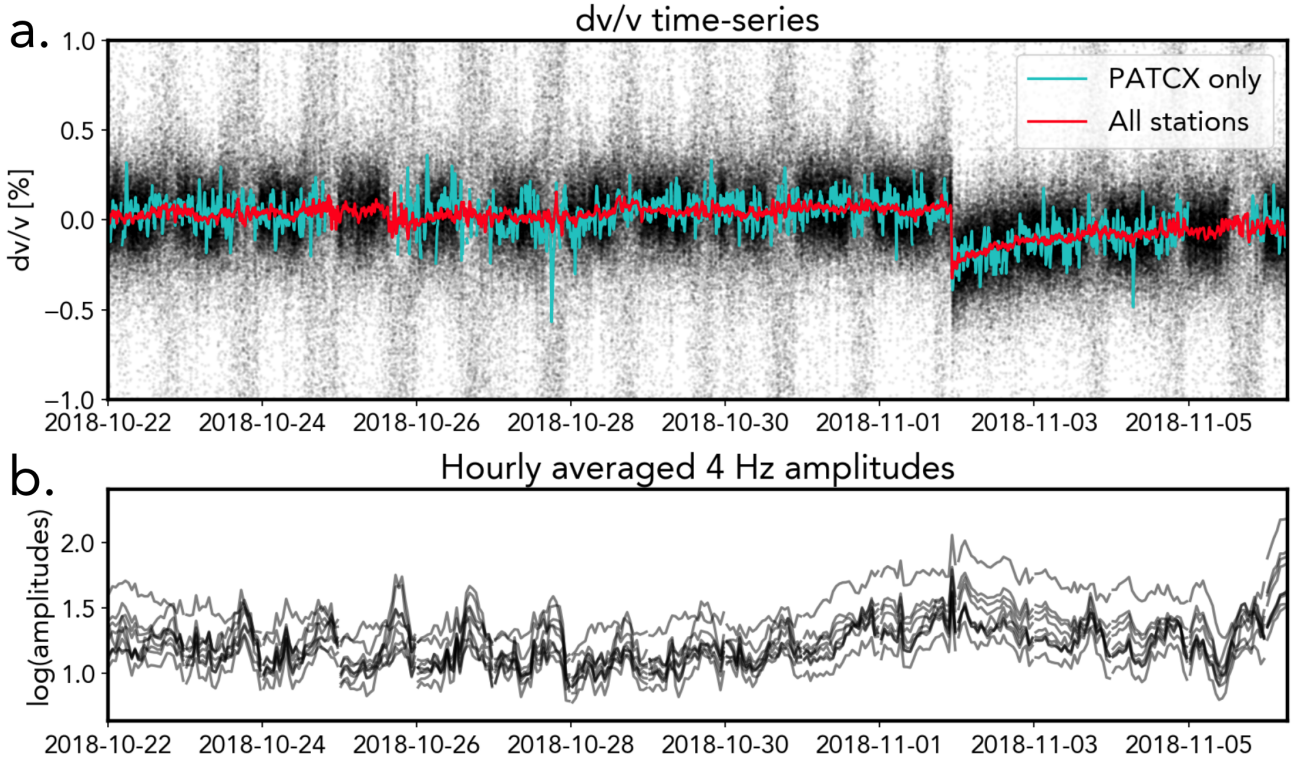
Figure 4. *PESO dv/v time-series.* **a.** Each black dot indicates an estimation using a single cross-correlation combination in the network. Blue line shows the joint result using the 6 self-combination of the PATCX station. Red line shows the results using all 405 combinations. Time resolution is 10 minutes. **b.** *Noise amplitudes time-series at 4 Hz.* Each lines represents the hourly logarithm of the hourly-averaged noise amplitudes for all the stations deployed during the 2 weeks. Opacity is a function of the curves overlap. Traces were processed with a 4 Hz Gaussian filter beforehand.

3.1.2 Stability of the measurement

We quantify the effect of multiple station averaging relative to the noise level in the final dv/v estimation. The standard deviation of the velocity time-series dv/v over all time samples of the 10 days prior to the earthquake can be plotted as a function of the stacking duration window and the number of combinations used (Fig. 5). Assuming that the velocity variations during this time-span is mostly due to noise, this standard deviation is a good proxy of the signal to noise ratio of (SNR) of the dv/v time-series and for the measurement stability. Because we exploit a late time-window (starting at 7 s, which corresponds to ~ 21 wavelengths at 3Hz, the lower limit of the used bandpass) in the correlation function for measuring the dv/v changes, we ensure to minimise diurnal physical changes that arise when processing earlier times (Richter et al. 2014; Sens-Schönfelder & Eulenfeld 2019). To construct the plot, we use all 6 self-correlations (AC+SC) for each of the ten stations. After shuffling the 60 combinations randomly in a list, we split them into multiple subsets corresponding to 6 (10 subsets), 10 (6 subsets), 15 (4 subsets), and 30 combinations (2 subsets). For each subset, we average the velocity changes using the similarity matrix stacking (equation 4) described in the methods (section 2.2) and extract the standard deviation of the obtained dv/v. We perform these calculations at several time resolution using different durations for the stacking window of the correlation functions ranging from 1 minute (no stacking) to 1 day stack. Finally, we also build the plots considering only the inner-ring stations (interstation distances from 260 to 670 m) and the outer-ring stations (interstation distances from 570 to 1580 m). The ring conventions are shown in Figure 1b.

The standard deviation always increases when using a lower number of combinations (Fig. 5a-c). For all curves, smaller stacking duration consistently also yields larger standard deviations. However, this deterioration systematically happens at different thresholds depending on the number of combinations used (Fig. 5a-c). This threshold is important as it drives the transition towards standard deviations that can be one order of magnitude higher at smaller time-resolution. Surprisingly, for large time windows, the average standard deviation of the outer ring stations (36 combinations, Fig. 5c) is smaller than the average using all combinations (Fig. 5a).

To illustrate the improvement of the estimations when using more stations, we plot the ratios between the standard deviations measured with many combinations (60, 24 and 36 combinations depending on the configuration) and the one measured with 6 combinations, which is the amount of information that would be obtained with one station (Fig. 5d-f). Theoretically, the reduction of the standard deviation of a sum of independent random variables with the same mean and variance should obey to a factor of $1/\sqrt{N}$ with N being the number of variables. For all combinations, we indicate this theoretical reduction using $N = 10$ (10 stations), $N = 4$ for the four inner ring stations and $N = 6$ for the six outer ring stations. We observe that the improvement of the dv/v result is not significant at both large time-windows and at small-time windows (Fig. 5d-f) for the three considered configurations. However, in an intermediate sweet spot, the ratios reach the theoretical reduction limit and even plot at lower values.
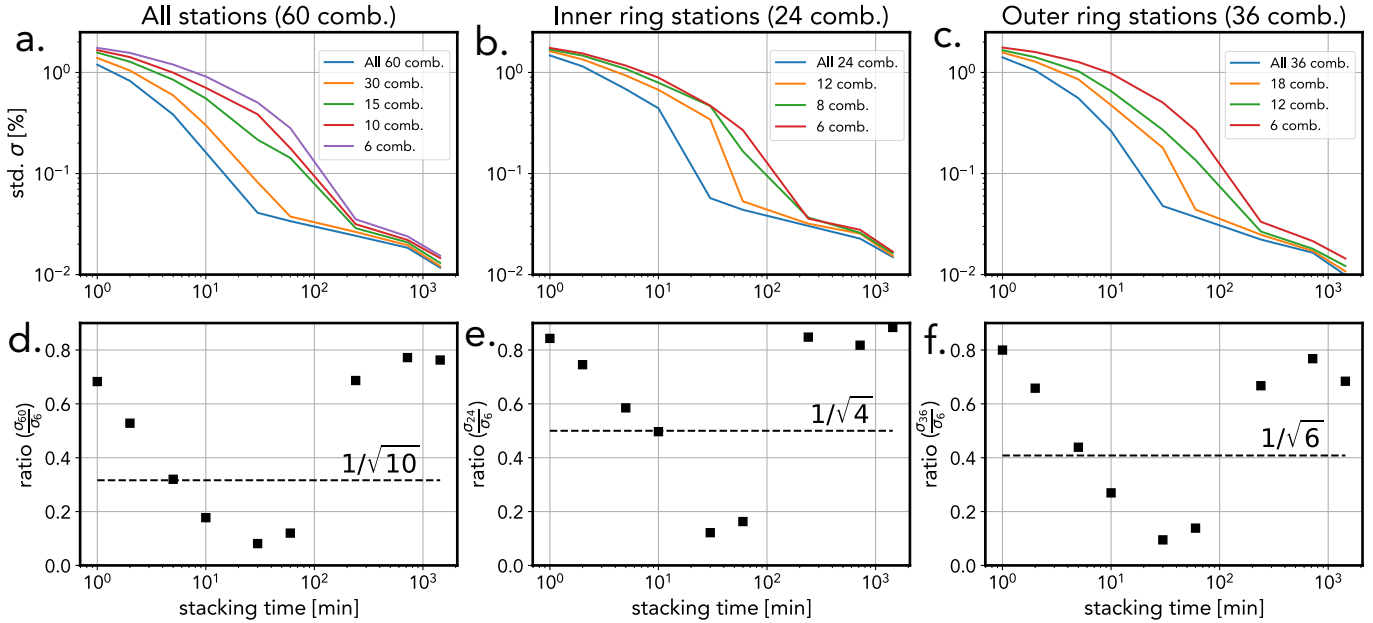
Figure 5. *Standard deviations of the* dv/v *changes prior to the earthquake (from the 22nd of October to the 1st of November) obtained using different stacking durations and number of combinations* **a.** Curves obtained using all single-combinations in the network. For each stacking duration, the mean of the standard deviation of the respective combination subset. The subsets are characterised by a number of combination shown as an inset label. We show on **b.** and **c.** the same plot but using only the inner ring stations and the outer ring stations respectively. The subplots **d**, **e** and **f** show the corresponding ratio between the standard deviation using all considered combinations and when using only six. The dashed line shows the theoretical reduction of the standard deviation for independent variables with the same mean and variance.
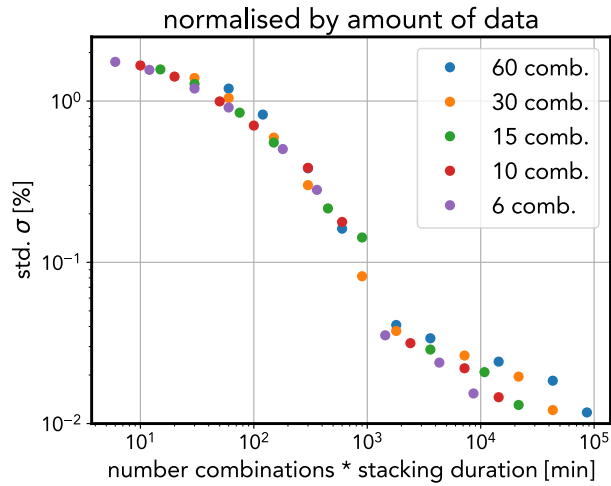
Figure 6. *Noise in the seismic velocity time-series normalised by the total amount of used seismic data.* Data are identical to Figure 5a but normalised by the total added length of the used seismic traces.

Finally, we normalised the standard deviations shown in Figure 5a by the amount of data used to obtain a velocity estimation. The resulting plot shows a remarkable collapse of the data point along a single non-linear decreasing trend (Fig. 6). Using our averaging method, the same signal to noise ratio can be achieved by either using more stations and smaller stacking time-windows or using less stations with more stacking, as long as the same amount of 'information' is used. Under these conditions, the ergodicity property can therefore be validated. Practically, this also means that a good precision can be obtained with one station at the cost of hav-

ing larger stacking time and therefore a lower time-resolution. We note that above the 10^3 minute mark, the standard deviations exhibit a step change and the agreement between the points is less striking. Knowing that small daily velocity changes due to temperature (Richter et al. 2014) or the Earth's tides (Sens-Schönfelder & Eulenfeld 2019) are active at the Patache field site, we attribute the degradation to physical effects that are more or less smoothed or averaged at large stacking times depending on the number of used combinations.

3.2 Shear velocity profile

The inverted 1D shear velocity profile is shown in Figure 7a along with the target dispersion curve which we inferred from the focal spot imaging technique 7c. The average shear velocities are in the 1250-2000 m/s range (mean = 1600) in the first ~ 200 m and in the 2400-3200 m/s range (mean=2750 m/s) in the ~ 250-1000 m depth range. The profile and the histogram of the layers depths is characterised by a clear two-layer structure (Fig. 7abd) with absolute seismic velocities indicating a hard-rock site. Most of inferred models result in smoother version of the target dispersion curve (Fig. 7c) with a noise level in the measurements estimated at a 25 m/s median value (Fig. 7e). The Vp/Vs ratio is poorly constrained but exhibits a median value of 1.58, typical of crystalline rocks or consolidated sediments (Mavko et al. 2009).

We note that the average velocity value inferred in the shallow surface ($\sim$1600 m/s) shows a rather good agreement with the apparent velocity ($\sim$1500-1600 m/s in the 4-6 Hz frequency range) inferred from the beamforming analysis performed to characterise the noise distribution (Fig. 1c). To refine the velocity profile, we performed a second inversion with the same method, adding the rough estimate of the high frequency phase velocity obtained from

the beamforming analysis (velocity at 1550 m/s at ∼4 Hz) to the target dispersion curve (Fig. S5). The obtained velocity profile emphasises the 2-layer structure with a discontinuity at ∼200 m depth and refines the shear velocity to 1550-1600 m/s in the superficial layer and ∼2750 m/s in the second layer. However, these secondary results should be interpreted with caution, as velocity measurement with beamforming may be flawed due to the potential steep incidence of body waves (Rost & Thomas 2002).

4   DISCUSSION

4.1   Conditions for stable velocity measurements

Finer time-resolution using passive seismic monitoring is a long standing challenge in seismic interferometry. Previous attempts to tackle this issue include denoising the cross-correlations with adaptative filters (Hadziioannou et al. 2011) or convolutional autoencoders (Viens & Van Houtte 2020), performing single-station cross-correlation at higher frequencies (Hobiger et al. 2014), stacking more short time-windows instead of a lower number of long time-windows (Xu et al. 2021) or tracking a persistent phase in the correlation functions (Lu & Ben-Zion 2022). In our study, we took the simple road of combining more stations for testing the ergodicity of the seismic velocity estimated from the noise wavefield.

The velocity change measurements were improved, with a noise level down to one order of magnitude lower than the one obtained with one station (6 combinations), depending on the length of the stacking window (Fig. 5). The theoretical limits plotted in Fig. 5d-f give a limited prediction of this improvement which indicates that our assumption of independent variables with the same mean and variance may not hold. However, at intermediate stacking length, the refinement of the results is clear (Fig. 5d-f). Outside of this intermediate range, the benefits are limited: With small stacking windows, the space-averaging is not sufficient to counterbalance the requirement of a minimum time duration for an effective statistical noise source summation (Fichtner et al. 2017). At the other end, with large stacking windows, the time-averaging is long enough for stable measurements and is not improved greatly when adding more stations. We conclude that the sweet spot between these conditions could be constrained with pilot deployments to optimise the number of stations needed for high-resolved temporal measurements. The plot of the dv/v recovery phase at different time resolutions highlights the trade-off between the choice of a time-resolution and the addition of noise in the time-series (Fig. 8). Ultimately, the ergodicity hypothesis was satisfied as long as the same amount of data was used (Fig. 6), suggesting that the stacking time of the correlation functions should be decided upon the number of available stations.

We found no significant effects when using different interstation distances (Fig. 5bc). However, the effects of this parameter should be investigated further because it is thought to be critical for optimised measurements as it controls the overall correlation of the observed wavefield at the different stations (relative to the targeted monitoring frequency). The largest correlation should be obtained when the interstation distance is on the order of the monitoring wavelength λ. At 3-6 Hz and using 1600 m/s for Rayleigh waves, we obtain $\lambda \sim 266 - 533$ m. With the 90-1600 m range in our array, we have therefore a mixture of correlated and uncorrelated arrivals. At large distances, the observed dv/v changes are also caused by different structural changes and the spatial averaging is not useful anymore.

Beyond methodological aspects, the monitoring of seismic velocity requires certain noise and structural conditions for stable measurements. Regarding noise source distribution, the reconstruction of the Green's function from correlations requires random and isotropic noise sources (Lobkis & Weaver 2001), a condition that is unlikely met in the field (Mulargia & Castellaro 2013). Nevertheless, a stable localised noise source is sufficient for monitoring purposes (Hadziioannou et al. 2009) and represents another ideal situation. In our frequency band, the beamforming analysis shows that the incoming energy has one dominant azimuthal direction (Fig. 1c). This feature suggests that the Peso field site is continuously excited by the same source which is likely to be induced by the surf of the ocean waves hitting the shoreline (Fig. S1). This stable situation is disturbed during windy afternoons, which cause the degradation of our velocity measurements (Fig. 4) due to high-amplitude arrivals. In our study, a statistical pre-processing scheme was designed to limit the disturbances from these deterministic signals. The 1D profile also suggests that a low velocity layer is present at the surface (Fig. 7ab) with elevated velocities (>1000 km/s for most of inferred models, Fig. 7a). Considering a low-velocity layer of $V_S = 1600$ m/s with a thickness $H = 200$ m, we can estimate an approximate resonance frequency with $f_k = ((2k+1)/4)/(V_S/H)$ (Nakamura 2000). With this relation, we obtain $f_0 \sim 2$ Hz to for the fundamental mode and $f_1 \sim 6$ Hz for the first overtone, these values being almost in the range of the 3-6 Hz band we used in this study. This configuration could promote the trapping and reverberation of seismic energy around this specific frequency band and with limited dissipation which are ideal conditions for monitoring subsurface changes (Sheng et al. 2021).

4.2   Relaxation in the field: timescales and geological structures

Following the 1st of November 2018 earthquake, we report a 0.4 % velocity reduction in the first 10 minutes after the earthquake. The observable slow dynamics behavior lasted roughly for ∼2 days and is well resolved at the 10-minute resolution (Fig. 4) with a characteristic log-linear recovery (Fig. 8). A minimum timescale of relaxation was not observed (Snieder et al. 2016; Shokouhi et al. 2017a) and if it exists, must be below our 10-minutes resolution. The dv/v time-series obtained at 1-minute resolution resolves an additional 0.1% drop at earlier relaxation times, albeit an increase in noise measurements according to previous analyses (grey line in Fig. 8). Such minute seismic-induced velocity changes in both amplitude (less than 0.5%) and timescale were not observed at this relatively high frequency band (3-6 Hz) to our knowledge. We used a late time window to ensure minimising source artefacts and sampling a large portion of the subsurface. Rapid velocity changes were also reported in the literature but often using different techniques that may be more prone to noise source changes and near-surface nonlinearity: Using very early times in autocorrelation functions during earthquake ground motion at frequencies above 10 Hz, the technique lead to comparatively larger changes (>5%) for very small PGV ($< 10^{-4}$ m/s) (Bonilla et al. 2019). Another remarkable time-series (at a 10-minute resolution) was obtained using P/S converted waves following the Mw 7.1 Ridgecrest earthquake (Lu & Ben-Zion 2022). However, their observed changes are larger than our results due to significant ground shaking. Our study suggests that small ground shaking induces a lingering effect that may be challenging to resolve. These effects matter for understanding the effect of cumulative aftershocks for the recovery of material properties af-
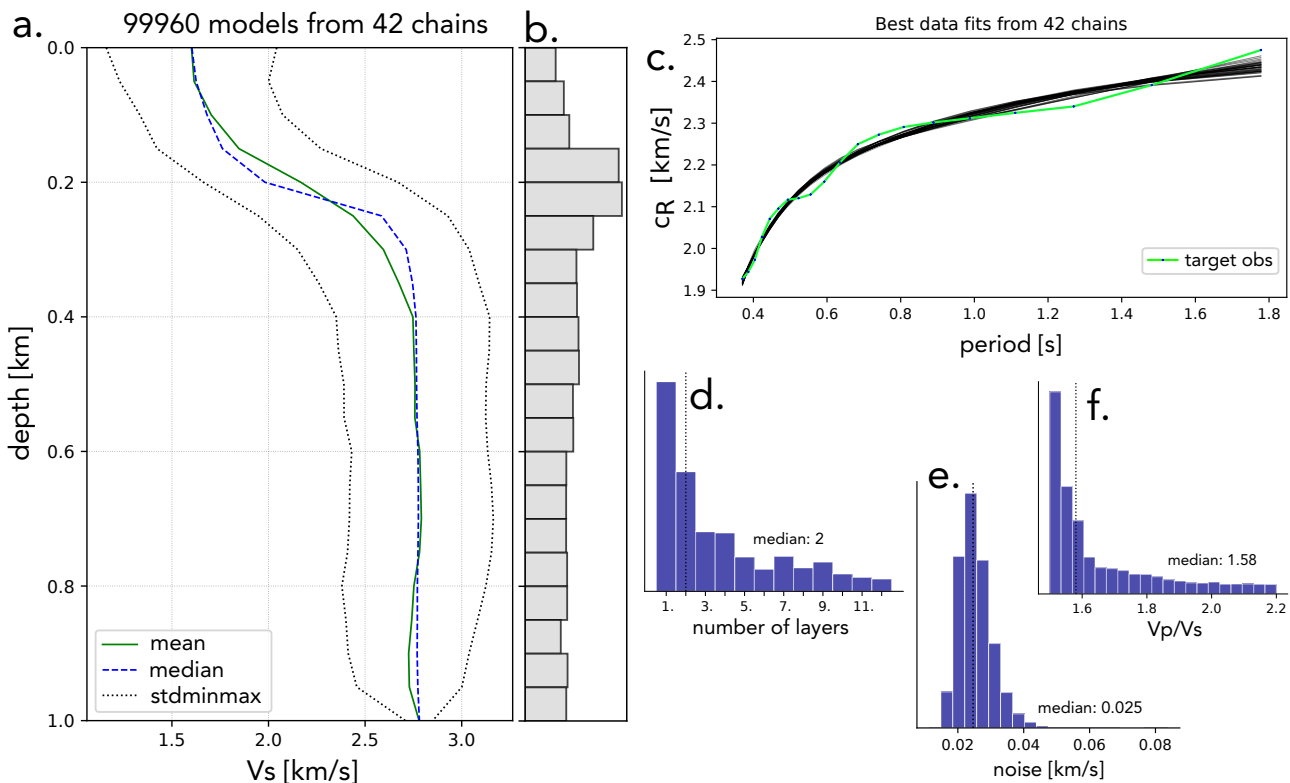
Figure 7. *Inversion of the 1D shear velocity profile and corresponding target dispersion curve.* **a.** Inferred shear velocity profile interpolated at a 50 m resolution. Green and blue lines shows the mean and the median value of the best retained models. Dashed black lines indicate the standard deviation. **b.** Histogram of the depth of the inferred layer structures **c.** The green line shows the dispersion curve that we use for the inversion, the other curves showing the best fit obtained for each chains . Histograms corresponding to the other inverted parameters are shown in **d.** for the number of layers, in **e.** for the noise level in the measurements and in **f.** for the Vp/Vs ratio.

ter large earthquakes (Sawazaki et al. 2018). Our temporal coverage was not sufficient to estimate the maximum relaxation timescale of the recovery. In a previous study we hypothesized that material properties and ambient conditions are the dominant control of the observable maximum relaxation time, rather than the co-seismic ground shaking intensity (Illien et al. 2022). A dynamic system analysis on a longer time-series could help us shed light on these controls and assumptions and is planned in a future manuscript.

In field studies, relaxation mechanisms are often interpreted as near-surface non-linearity induced by soils deformation (Sleep & Nakata 2017; Viens et al. 2018; Guéguen et al. 2019). Pictures from the field (Fig. S6) indicate the presence of a conglomerate with evaporites at the surface, which may constitute the first 200 m layer (Fig. 7a). If we assume the dominance of Rayleigh wave energy in the noise wavefield, the corresponding sensitivity kernel associated with the measured dispersion curve (Fig. 7c) and the inferred 1D model (Fig. 7a) suggest that these rocks host the observed velocity changes at frequencies above 3 Hz (Fig S7). The higher velocity in the second layer could correspond to crystalline rocks such as gabbros, according to geological studies in the area (Tapia et al. 2018). In the laboratory, relaxation has been observed in crystalline (Shokouhi et al. 2020; Meyer et al. 2021) and sedimentary rocks (Brantut 2015). Numerical simulations and experiments suggests that the largest contact areas in the rock fractures (Shokouhi et al. 2020), cracks (Gao et al. 2019), and the grain contacts in granular media (Kober et al. 2022) controls the relaxation timescale. Due to higher strength, hard rocks can sustain larger flaws and fractures, which in turn may lead to longer relaxation timescale due to high
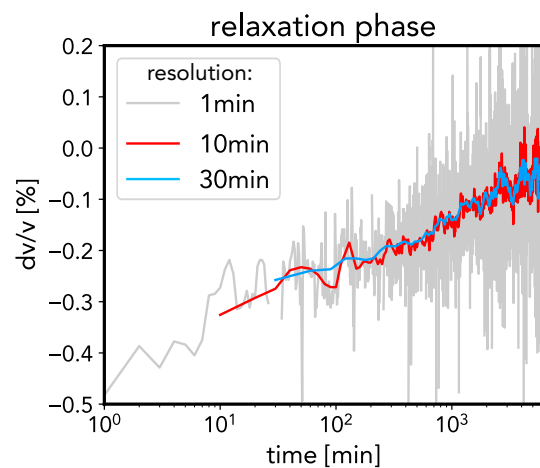
Figure 8. *Relaxation phase recorded by the PESO array at different resolutions.* The recovery phase shown in Fig. 4 using all the combinations is plotted in red. The log-linear x-axis emphasises the characteristic slow dynamics recovery. Note the variation of noise at high-resolution (dt = 1 minute) and at lower resolution (dt = 30 minutes).

activation barriers. This statement may only be valid if slow dynamics behaviour effectively originates due to thermally-activated processes such as with the Arrhenius equation (Snieder et al. 2016; Ostrovsky et al. 2019).

5   CONCLUSIONS

In this study, we explored the potential advantage of using more co-located stations to improve the time resolution of relative seismic velocity changes dv/v inferred from ambient noise correlations. We made the assumption that the dv/v estimation obeys the ergodic hypothesis i.e the time-average (one station with large stacking time for the correlation functions) is equal to the space-average (several stations with small stacking time for correlation functions). We found that the staking time required to obtain stable correlation functions and therefore velocity measurements can be significantly lowered by using more stations. When normalised by the amount of used seismic data, the ergodicity was satisfied, which suggests that the minimum time-resolution of dv/v measurements is a function of the number of available stations. What is the highest time-resolution limit that one can reach ? This question remains to be answered but our study demonstrates an important property of seismic interferometry from ambient noise correlations.

Thanks to the gained precision, we resolved a 0.4% velocity drop after a seismic event that induced ∼1 cm/s of PGV at a 10-minutes resolution. Half of this drop was then recovered with a log-linear relaxation shape in agreement with slow dynamics studies. The largest changes were contained in the immediate aftermath of the earthquake. We showed that this relaxation behaviour is happening in a hard rock site according to the local 1D shear velocity profile we derived from the focal spot imaging technique and an McMC transdimensional Bayesian inversion.

DATA AVAILABILITY

The data from the PESO network will be made available at the GEOFON archive as soon as the paper will be published. The data from the PATCX station are already accessible at the following DOI:10.14470/PK615318.

REFERENCES

Albaric, J., Kühn, D., Ohrnberger, M., Langet, N., Harris, D., Polom, U., Lecomte, I., & Hillers, G., 2021. Seismic monitoring of permafrost in svalbard, arctic norway, *Seismological Research Letters*, **92**(5), 2891–2904.

Bekele, A., Birgisson, B., Ryden, N., & Gudmarsson, A., 2017. Slow dynamic diagnosis of asphalt concrete specimen to determine level of damage caused by static low temperature conditioning, *AIP Conference Proceedings*, **1806**, 1–7.

Bittner, J. A. & Popovics, J. S., 2021. Mechanistic diffusion model for slow dynamic behavior in materials, *Journal of the Mechanics and Physics of Solids*, **150**(February), 104355.

Bodin, T., Sambridge, M., Tkalčić, H., Arroucau, P., Gallagher, K., & Rawlinson, N., 2012. Transdimensional inversion of receiver functions and surface wave dispersion, *Journal of Geophysical Research: Solid Earth*, **117**(2), 1–24.

Bonilla, L. F., Guéguen, P., & Ben-Zion, Y., 2019. Monitoring coseismic temporal changes of shallow material during strong ground motion with interferometry and autocorrelation, *Bulletin of the Seismological Society of America*, **109**(1), 187–198.

Brantut, N., 2015. Time-dependent recovery of microcrack damage and seismic wave speeds in deformed limestone, *Journal of Geophysical Research: Solid Earth*, **120**(12), 8088–8109.

Brenguier, F., Campillo, M., Hadziioannou, C., Shapiro, N. M., Nadeau, R. M., & Larose, E., 2008. Postseismic relaxation along the San Andreas fault at Parkfield from continuous seismological observations., *Science (New York, N.Y.)*, **321**(5895), 1478–81.

Budi-Santoso, A. & Lesage, P., 2016. Velocity variations associated with the large 2010 eruption ofMerapi volcano, Java, retrieved from seismic multiplets and ambient noise cross-correlation, *Geophysical Journal International*, **206**(1), 221–240.

Clements, T. & Denolle, M. A., 2018. Tracking Groundwater Levels Using the Ambient Seismic Field, *Geophysical Research Letters*, **45**(13), 6459–6465.

Conti, S., Roux, P., & Fink, M., 2002. Depth and range shifting of a focal spot using a time-reversal mirror in an acoustic waveguide, *Applied Physics Letters*, **80**(19), 3647–3649.

Dietze, M., Cook, K. L., Illien, L., Rach, O., Puffpaff, S., Stodian, I., & Hovius, N., 2020. Impact of Nested Moisture Cycles on Coastal Chalk Cliff Failure Revealed by Multiseasonal Seismic and Topographic Surveys, *Journal of Geophysical Research: Earth Surface*, **125**(8).

Donaldson, C., Winder, T., Caudron, C., & White, R. S., 2019. Crustal seismic velocity responds to a magmatic intrusion and seasonal loading in Iceland's Northern Volcanic Zone, *Science Advances*, **5**(11).

Dreiling, J. & Tilmann, F., 2019. BayHunter - McMC transdimensional Bayesian inversion of receiver functions and surface wave dispersion.

Dreiling, J., Tilmann, F., Yuan, X., Haberland, C., & Seneviratne, S. W., 2020. Crustal Structure of Sri Lanka Derived From Joint Inversion of Surface Wave Dispersion and Receiver Functions Using a Bayesian Approach, *Journal of Geophysical Research: Solid Earth*, **125**(5), 1–15.

Fichtner, A., Stehly, L., Ermert, L., & Boehm, C., 2017. Generalized interferometry - I: Theory for interstation correlations, *Geophysical Journal International*, **208**(2), 603–638.

Fink, M., 2008. Time-reversal acoustics, *Journal of Physics: Conference Series*, **118**(1).

Gao, K., Rougier, E., Guyer, R. A., Lei, Z., & Johnson, P. A., 2019. Simulation of crack induced nonlinear elasticity using the combined finite-discrete element method, *Ultrasonics*, **98**, 51–61.

Gao, L., Shokouhi, P., & Rivière, J., 2022. Effect of relative humidity on the nonlinear elastic response of granular media, *Journal of Applied Physics*, **131**(5).

Gassenmeier, M., Sens-Schönfelder, C., Delatre, M., & Korn, M., 2015. Monitoring of environmental influences on seismic velocity at the geological storage site for CO2 in Ketzin (Germany) with ambient seismic noise, *Geophysical Journal International*, **200**(1), 524–533.

Gassenmeier, M., Sens-Schönfelder, C., Eulenfeld, T., Bartsch, M., Victor, P., Tilmann, F., & Korn, M., 2016. Field observations of seismic velocity changes caused by shaking-induced damage and healing due to mesoscopic nonlinearity, *Geophysical Journal International*, **204**(3), 1490–1502.

GFZ Potsdam & CNRS-INSU, 2006. Ipoc seismic network.

Groos, J. C. & Ritter, J. R. R., 2009. Time domain classification and quantification of seismic noise in an urban environment, *Geophysical Journal International*, **179**(2), 1213–1231.

Guéguen, P., Bonilla, L. F., & Douglas, J., 2019. Comparison of soil nonlinearity (in situ stress-strain relation and G/G max Reduction) observed in strong-motion databases and modeled in ground-motion prediction equations, *Bulletin of the Seismological Society of America*, **109**(1), 178–186.

Guyer, R. A., Ten Cate, J., & Johnson, P., 1999. Hysteresis and the dynamic elasticity of consolidated granular materials, *Physical Review Letters*, **82**(16), 3280–3283.

Hadziioannou, C., Larose, E., Coutant, O., Roux, P., & Campillo, M., 2009. Stability of monitoring weak changes in multiply scattering media with ambient noise correlation: Laboratory experiments, *The Journal of the Acoustical Society of America*, **125**(6), 3688–3695.

Hadziioannou, C., Larose, E., Baig, A., Roux, P., & Campillo, M., 2011. Improving temporal resolution in ambient noise monitoring of seismic wave speed, *Journal of Geophysical Research: Solid Earth*, **116**(7), 1–10.

Hillers, G., Roux, P., Campillo, M., & Ben-Zion, Y., 2016. Focal spot imaging based on zero lag cross-correlation amplitude fields: Application to dense array data at the San Jacinto fault zone, *Journal of Geophysical Research: Solid Earth*, **121**(11), 8048–8067.

Hobiger, M., Wegler, U., Shiomi, K., & Nakahara, H., 2014. Single-station

cross-correlation analysis of ambient seismic noise: application to stations in the surroundings of the 2008 Iwate-Miyagi Nairiku earthquake, *Geophysical Journal International*, **198**(1), 90–109.

Illien, L., Andermann, C., Sens-Schönfelder, C., Cook, K. L., Baidya, K. P., Adhikari, L. B., & Hovius, N., 2021. Subsurface Moisture Regulates Himalayan Groundwater Storage and Discharge, *AGU Advances*, **2**(2).

Illien, L., Sens-Schönfelder, C., Andermann, C., Marc, O., Cook, K. L., Adhikari, L. B., & Hovius, N., 2022. Seismic Velocity Recovery in the Subsurface: Transient Damage and Groundwater Drainage Following the 2015 Gorkha Earthquake, Nepal, *Journal of Geophysical Research: Solid Earth*, **127**(2), 1–18.

Knight, J. B., Fandrich, C. G., Ning Lau, C., Jaeger, H. M., & Nagel, S. R., 1995. Density relaxation in a vibration.pdf, *Physical Review E*, **51**(5).

Kober, J., Gliozzi, A., Scalerandi, M., & Tortello, M., 2022. Material Grain Size Determines Relaxation-Time Distributions in Slow-Dynamics Experiments, *Physical Review Applied*, **17**(1), 1.

Lecocq, T., Longuevergne, L., Pedersen, H. A., Brenguier, F., & Stammler, K., 2017. Monitoring ground water storage at mesoscale using seismic noise: 30 years of continuous observation and thermo-elastic and hydrological modeling, *Scientific Reports*, **7**(1).

Lieou, C. K., Daub, E. G., Ecke, R. E., & Johnson, P. A., 2017. Slow Dynamics and Strength Recovery in Unconsolidated Granular Earth Materials: A Mechanistic Theory, *Journal of Geophysical Research: Solid Earth*, **122**(10), 7573–7583.

Lindner, F., Wassermann, J., & Igel, H., 2021. Seasonal Freeze-Thaw Cycles and Permafrost Degradation on Mt. Zugspitze (German/Austrian Alps) Revealed by Single-Station Seismic Monitoring, *Geophysical Research Letters*, **48**(18), 1–11.

Lobkis, O. I. & Weaver, R. L., 2001. On the emergence of the Green's function in the correlations of a diffuse field, *The Journal of the Acoustical Society of America*, **110**(6), 3011–3017.

Lu, Y. & Ben-Zion, Y., 2022. Regional seismic velocity changes following the 2019 Mw7.1 Ridgecrest, California earthquake from autocorrelations and P/S converted waves, *Geophysical Journal International*, **228**(1), 620–630.

Manga, M., Beresnev, I., Brodsky, E. E., Elkhoury, J. E., Elsworth, D., Ingebritsen, S. E., Mays, D. C., & Wang, C. Y., 2012. Changes in permeability caused by transient stresses: Field observations, experiments, and mechanisms, *Reviews of Geophysics*, **50**(2).

Marc, O., Hovius, N., Meunier, P., Uchida, T., & Hayashi, S., 2015. Transient changes of landslide rates after earthquakes, *Geology*, **43**(10), 883–886.

Marc, O., Sens-Schönfelder, C., Illien, L., Meunier, P., Hobiger, M., Sawazaki, K., Rault, C., & Hovius, N., 2021. Toward Using Seismic Interferometry to Quantify Landscape Mechanical Variations after Earthquakes, *Bulletin of the Seismological Society of America*, pp. 1–19.

Mavko, G., Mukerji, T., & Dvorkin, J., 2009. *The Rock Physics Handbook: Tools for Seismic Analysis of Porous Media*, Cambridge University Press, 2nd edn.

McNicol, R., 1949. The fading of radio waves of medium and high frequencies, *Proceedings of the IEE - Part III: Radio and Communication Engineering*, **96**(44), 517–524.

Meyer, G. G., Brantut, N., Mitchell, T. M., Meredith, P. G., & Plümper, O., 2021. Time Dependent Mechanical Crack Closure as a Potential Rapid Source of Post-Seismic Wave Speed Recovery: Insights From Experiments in Carrara Marble, *Journal of Geophysical Research: Solid Earth*, **126**(4), 1–29.

Moore, C. C., 2015. Ergodic theorem, ergodic theory, and statistical mechanics, *Proceedings of the National Academy of Sciences of the United States of America*, **112**(7), 1907–1911.

Mulargia, F. & Castellaro, S., 2013. A seismic passive imaging step beyond SPAC and ReMi, *Geophysics*, **78**(5).

Nakamura, Y., 2000. Clear identification of fundamental idea of Nakamura's technique and its applications, *Proceedings of the 12th world conference on . . .* , p. Paper no. 2656.

Nakata, N. & Snieder, R., 2012. Estimating near-surface shear wave velocities in Japan by applying seismic interferometry to KiK-net data, *Journal of Geophysical Research: Solid Earth*, **117**(1).

Oakley, D. O., Forsythe, B., Gu, X., Nyblade, A. A., & Brantley, S. L., 2021. Seismic Ambient Noise Analyses Reveal Changing Temperature and Water Signals to 10s of Meters Depth in the Critical Zone, *Journal of Geophysical Research: Earth Surface*, **126**(2), 1–21.

Oshima, M. & Takenaka, H., 2020. A P-and S-wave picking technique based on the probabilistic density function of seismic-waveform amplitude, *Bulletin of the Seismological Society of America*, **110**(2), 763–782.

Ostrovsky, L., Lebedev, A., Riviere, J., Shokouhi, P., Wu, C., Stuber Geesey, M. A., & Johnson, P. A., 2019. Long-Time Relaxation Induced by Dynamic Forcing in Geomaterials, *Journal of Geophysical Research: Solid Earth*, **124**(5), 5003–5013.

Overduin, P. P., Haberland, C., Ryberg, T., Kneier, F., Jacobi, T., Grigoriev, M. N., & Ohrnberger, M., 2015. Submarine permafrost depth from ambient seismic noise, *Geophysical Research Letters*, **42**(18), 7581–7588.

Qin, L., Ben-Zion, Y., Bonilla, L. F., & Steidl, J. H., 2020. Imaging and Monitoring Temporal Changes of Shallow Seismic Velocities at the Garner Valley Near Anza, California, Following the M7.2 2010 El Mayor-Cucapah Earthquake, *Journal of Geophysical Research: Solid Earth*, **125**(1), 1–17.

Remillieux, M. C., Ulrich, T. J., Goodman, H. E., & Ten Cate, J. A., 2017. Propagation of a Finite-Amplitude Elastic Pulse in a Bar of Berea Sandstone: A Detailed Look at the Mechanisms of Classical Nonlinearity, Hysteresis, and Nonequilibrium Dynamics, *Journal of Geophysical Research: Solid Earth*, **122**(11), 8892–8909.

Richter, T., Sens-Schönfelder, C., Kind, R., & Asch, G., 2014. Comprehensive observation and modeling of earthquake and temperature-related seismic velocity changes in northern Chile with passive image interferometry, *Journal of Geophysical Research: Solid Earth*, **119**(6), 4747–4765.

Rivet, B., Girin, L., & Jutten, C., 2007. Log-rayleigh distribution: A simple and efficient statistical representation of log-spectral coefficients, *IEEE Transactions on Audio, Speech and Language Processing*, **15**(3), 796–802.

Rost, S. & Thomas, C., 2002. Array seismology: Methods and applications, *Reviews of Geophysics*, **40**(3), 2–1–2–27.

Sawazaki, K., Saito, T., & Shiomi, K., 2018. Shallow Temporal Changes in S Wave Velocity and Polarization Anisotropy Associated With the 2016 Kumamoto Earthquake Sequence, Japan, *Journal of Geophysical Research: Solid Earth*, **123**(11), 9899–9913.

Sens-Schönfelder, C. & Brenguier, F., 2019. Noise-based Monitoring, in *Seismic Ambient Noise*, chap. Noise-base, pp. 267–301, eds Nakata, N., Gualtieri, L., & Fichtner, A., Cambridge University Press.

Sens-Schönfelder, C. & Eulenfeld, T., 2019. Probing the in situ Elastic Nonlinearity of Rocks with Earth Tides and Seismic Noise, *Physical Review Letters*, **122**(13).

Sens-Schönfelder, C. & Wegler, U., 2006. Passive image interferometry and seasonal variations of seismic velocities at Merapi Volcano, Indonesia, *Geophysical Research Letters*, **33**(21).

Sens-Schönfelder, C., Pomponi, E., & Peltier, A., 2014. Dynamics of Piton de la Fournaise volcano observed by passive image interferometry with multiple references, *Journal of Volcanology and Geothermal Research*, **276**, 32–45.

Sens-Schönfelder, C., Snieder, R., & Li, X., 2019. A model for nonlinear elasticity in rocks based on friction of internal interfaces and contact aging, *Geophysical Journal International*, **216**(1), 319–331.

Sheng, Y., Ellsworth, W. L., Lellouch, A., & Beroza, G. C., 2021. Depth Constraints on Coseismic Velocity Changes From Frequency-Dependent Measurements of Repeating Earthquake Waveforms, *Journal of Geophysical Research: Solid Earth*, **126**(2), 1–12.

Shokouhi, P., Rivière, J., Guyer, R. A., & Johnson, P. A., 2017a. Slow dynamics of consolidated granular systems: Multi-scale relaxation, *Applied Physics Letters*, **111**(25).

Shokouhi, P., Rivière, J., Guyer, R. A., & Johnson, P. A., 2017b. Slow dynamics of consolidated granular systems: Multi-scale relaxation, *Applied Physics Letters*, **111**(25).

Shokouhi, P., Jin, J., Wood, C., Rivière, J., Madara, B., Elsworth, D., & Marone, C., 2020. Dynamic Stressing of Naturally Fractured Rocks:

On the Relation Between Transient Changes in Permeability and Elastic Wave Velocity, *Geophysical Research Letters*, **47**(1), 1–10.

Sleep, N. H. & Nakata, N., 2017. Nonlinear attenuation of S waves by frictional failure at shallow depths, *Bulletin of the Seismological Society of America*, **107**(4), 1828–1848.

Snieder, R., Sens-Schönfelder, C., & Wu, R., 2016. The time dependence of rock healing as a universal relaxation process, a tutorial, *Geophysical Journal International*, **208**(1), 1–9.

Takano, T., Nishimura, T., Nakahara, H., Ohta, Y., & Tanaka, S., 2014. Seismic velocity changes caused by the Earth tide: Ambient noise correlation analyses of small-array data, *Geophysical Research Letters*, **41**(17), 6131–6136.

Tapia, J., González, R., Townley, B., Oliveros, V., Álvarez, F., Aguilar, G., Menzies, A., & Calderón, M., 2018. Geology and geochemistry of the Atacama Desert, *Antonie van Leeuwenhoek, International Journal of General and Molecular Microbiology*, **111**(8), 1273–1291.

TenCate, J. A., Smith, E., & Guyer, R. A., 2000. Universal slow dynamics in granular solids, *Physical Review Letters*, **85**(5), 1020–1023.

Viens, L. & Van Houtte, C., 2020. Denoising ambient seismic field correlation functions with convolutional autoencoders, *Geophysical Journal International*, **220**(3), 1521–1535.

Viens, L., Denolle, M. A., Hirata, N., & Nakagawa, S., 2018. Complex Near-Surface Rheology Inferred From the Response of Greater Tokyo to Strong Ground Motions, *Journal of Geophysical Research: Solid Earth*, **123**(7), 5710–5729.

Xu, Y., Lebedev, S., Meier, T., Bonadio, R., & Bean, C. J., 2021. Optimized workflows for high-frequency seismic interferometry using dense arrays, *Geophysical Journal International*, **227**(2), 875–897.

Yoritomo, J. Y. & Weaver, R. L., 2020. Slow dynamics in a single glass bead, *Physical Review E*, **101**(1), 1–14.

Supplementary material to

Resolving minute temporal seismic velocity changes induced by earthquake damage: The more stations, the merrier ?

Luc Illien[1,2], Christoph Sens-Schönfelder[1], Kuan-Yu Ke[1,3]

[1] *Helmholtz Center, German Center for Geosciences GFZ, Potsdam, Germany*

[2] *Department of Geosciences, Potsdam Universität, Potsdam, Germany*

[3] *Insitut fur geologische Wissenschaften, Freie Universität Berlin, Berlin, Germany*

17 October 2022

1 TEXT S1: BEAMFORMING

To investigate the character of the wavefield used to monitor the velocity changes we apply plane-wave beamforming to the noise recorded with the array in the 4 - 6 Hz band. We use instrument corrected data from October 22nd for an F-K analysis of 10s long time windows with 50% overlap. Analysis is implemented using the Obspy array processing routine. From each of the 10s long segments we infer the slowness vector with the maximum energy. Figure 1c of the main text shows the probability distribution of the resulting slowness vectors. Energy in this frequency band is strongly dominated by waves with a slowness of 0.65 s/km striking the network from south-west.

2 FIGURES S*

Figure 1. *Screenshot of the array in Google Earth.* The yellow pins stand for the PESO stations. The picture highlights the cliff escarpment. The shoreline orientation is in agreement with the beamforming results in which the noise strikes the array from a south-west direction.

REFERENCES

Herrmann, R. B. & Ammon, C. J., 2002. Computer programs in seismology: Surface waves, receiver functions and crustal structure, *St. Louis University, St. Louis, MO*, **25**, 46.

Sens-Schönfelder, C. & Eulenfeld, T., 2019. Probing the in situ Elastic Nonlinearity of Rocks with Earth Tides and Seismic Noise, *Physical Review Letters*, **122**(13).
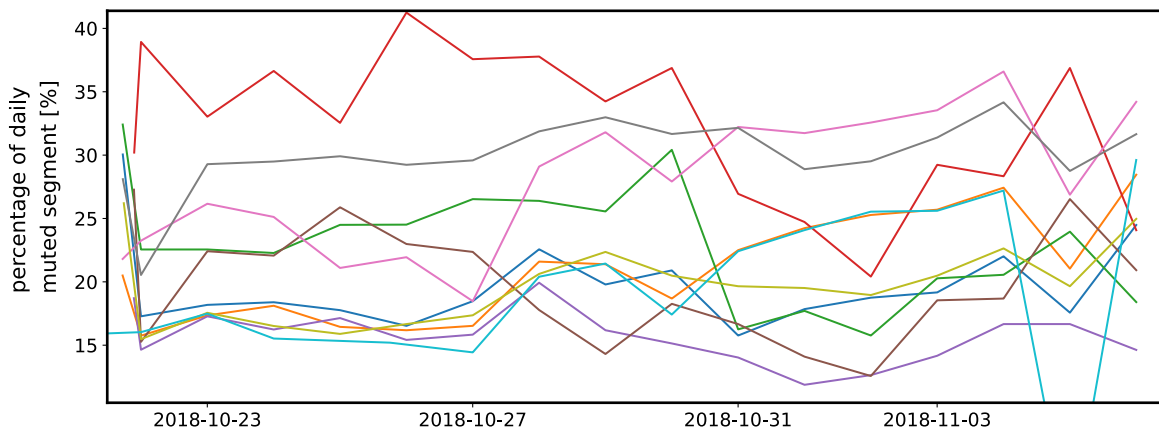
Figure 2. *Proportion of daily muted segments.* Each color stands for a different station.
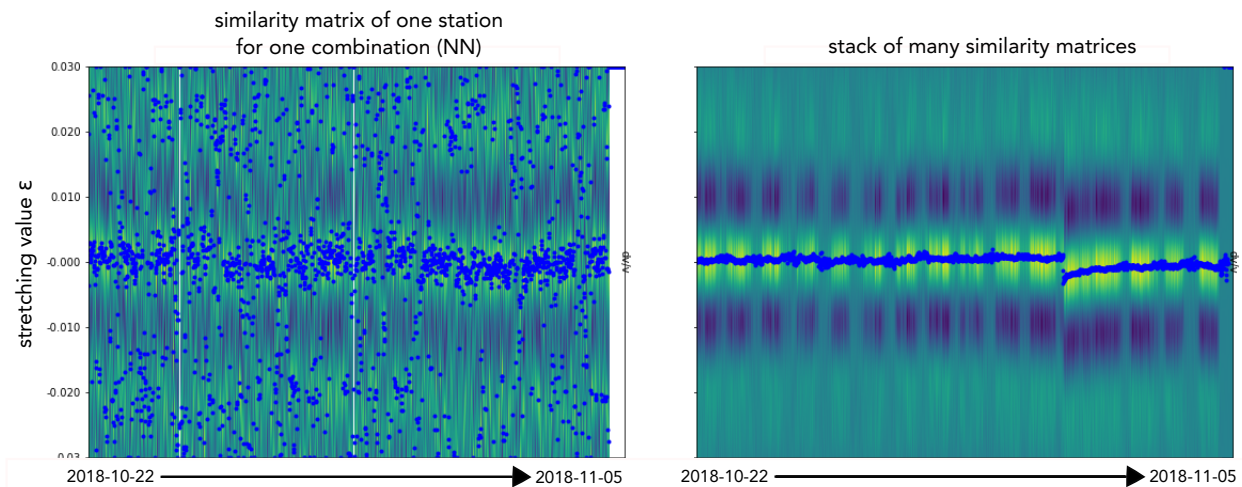
Figure 3. *Illustration of the similarity matrix.* On the left, we report the similarity matrix when using only one autocorrelation at one station. The blue dots show the stretching value corresponding to the best correlation values in the equation (4) of the main text. On the right, we show the similarity matrix built when stacking all the possible matrices (such as the one on the left) of the network. The figure illustrates the enhancement of the measure using this technique.
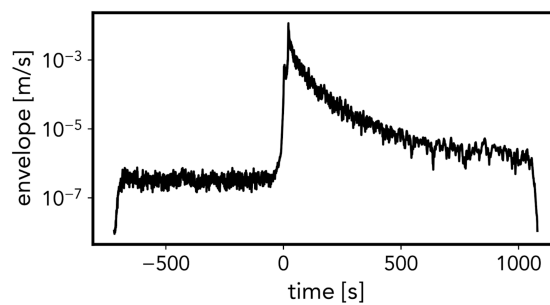
Figure 4. *Average envelope of the horizontal components in the network during coseismic ground shaking.* The time 0 corresponds to the onset of the P-wave. The envelope is averaged over all the network.
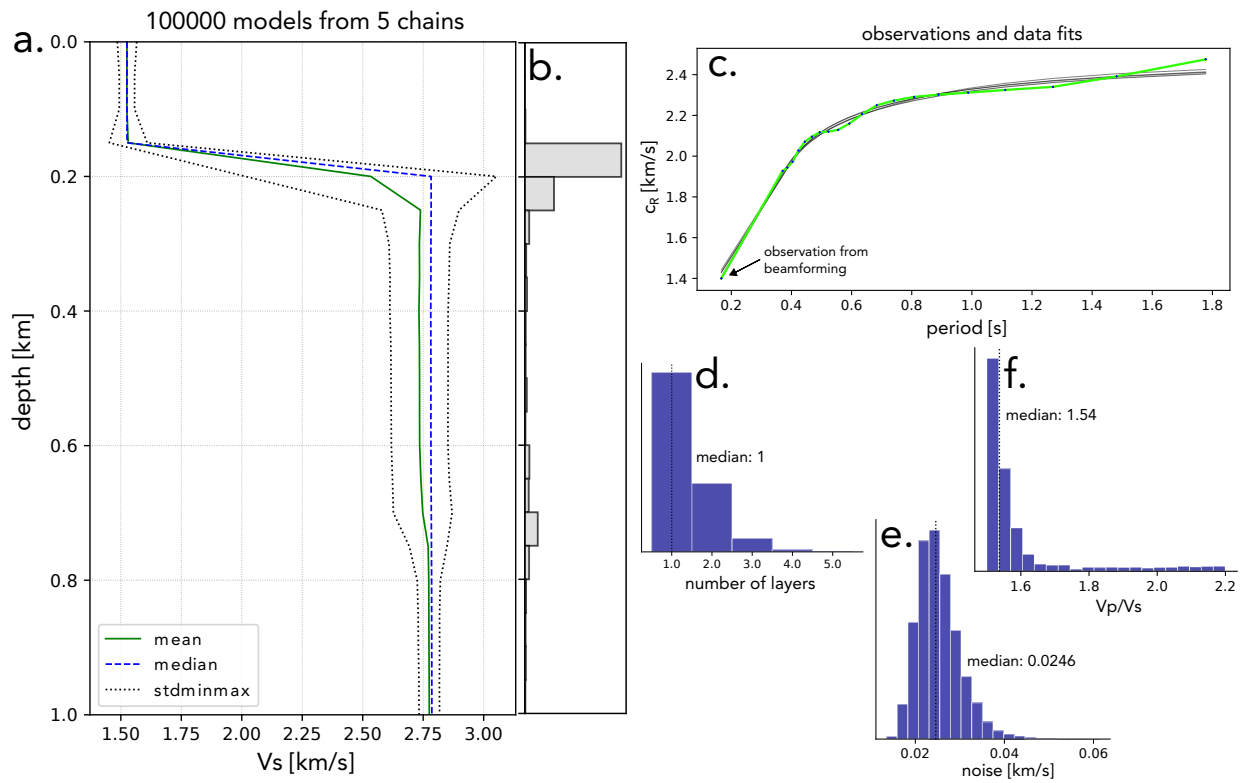
Figure 5. *Inversion results when adding the observation from the beamforming method.* **a.** Inferred shear velocity profile interpolated at a 50 m resolution. Green and blue lines shows the mean and the median value of the best retained models. Dashed black lines indicated the standard deviation. **b.** Histogram of the depth of the inferred layer structures **c.** The green line shows the dispersion curve that we use for the inversion, the other curves showing the best fit obtained for each chains. Histograms corresponding to the other inverted parameters are shown in **d.** for the number of layers, in **e.** for the noise level in the measurements and in **f.** for the Vp/Vs ratio.
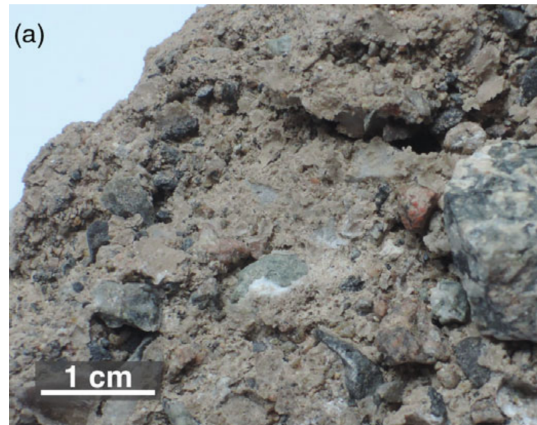
Figure 6. *Geological media observed in the field.* The geology hints at clasts embedded in a matrix containing large amounts of evaporites (likely gypsum and halite). The picture is taken from the study of Sens-Schönfelder & Eulenfeld (2019).
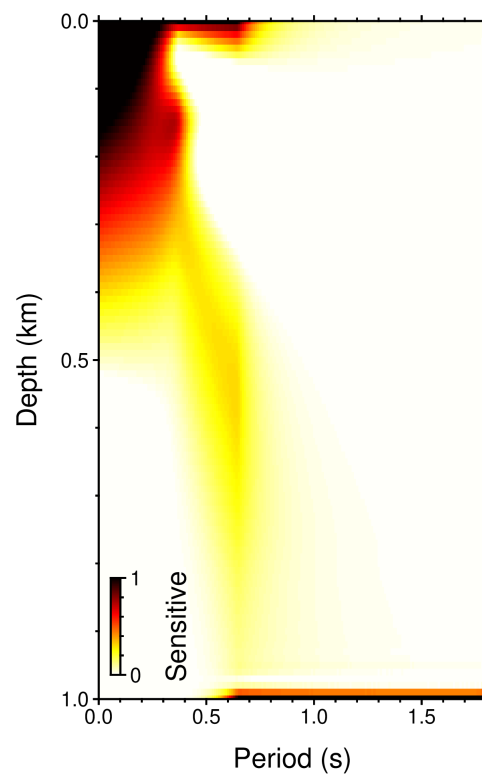
Figure 7. *Rayleigh wave sensitivity given the inferred 1D profile and the measured dispersion curve.* The kernel was computed using the CPS software (Herrmann & Ammon 2002).